Amorphous calcium phosphate is a major component of the forming fin bones of zebrafish: Indications for an amorphous precursor phase

Julia Mahamid*, Amnon Sharir†, Lia Addadi*‡, and Steve Weiner*

*Department of Structural Biology, Weizmann Institute of Science, and †Koret School of Veterinary Medicine, Hebrew University of Jerusalem, 76100 Rehovot, Israel

Edited by William Landis, Northeastern Ohio Universities, and accepted by the Editorial Board July 18, 2008 (received for review April 6, 2008)

A fundamental question in biomineralization is the nature of the first-formed mineral phase. In vertebrate bone formation, this issue has been the subject of a long-standing controversy. We address this key issue using the continuously growing fin bony rays of the Tuebingen long-fin zebrafish as a model for bone mineralization. Employing high-resolution scanning and transmission electron microscopy imaging, electron diffraction, and elemental analysis, we demonstrate the presence of an abundant amorphous calcium phosphate phase in the newly formed fin bones. The extracted amorphous mineral particles crystallize with time, and mineral crystallinity increases during bone maturation. Based on these findings, we propose that this amorphous calcium phosphate phase may be a precursor phase that later transforms into the mature crystalline mineral.

biomineralization | fish fin

Many invertebrates from different phyla build their mineralized skeletons by first depositing an amorphous disordered mineral precursor that subsequently transforms into a crystalline phase (1–6). Whether or not vertebrate mineralization proceeds in this manner, has been the subject of a long-standing debate (7–15). Mature bone mineral is a highly substituted crystalline phase of calcium phosphate called carbonated hydroxyapatite (16). It forms in the shape of nanometer-size irregular platelets with a very high surface area (17). The crystals are initially observed mainly in the gap regions of aligned type I collagen fibrils constituting the bone organic matrix and grow with their *c*-axes oriented along the long axis of the collagen fibril (16, 18). This pattern of mineral deposition is the hallmark of bone materials (19, 20). *In vitro*, at neutral pH and moderate supersaturation, amorphous calcium phosphate (ACP) is often the first-formed deposit. Under these conditions, ACP transforms into octacalcium phosphate (OCP), which in turn transforms into the thermodynamically more stable hydroxyapatite (21). Recently, collagen mineralization via a transient amorphous calcium phosphate phase was shown *in vitro* to produce aligned intrafibrillar carbonated apatite crystals (15). Identification of the initial mineral phase deposited *in vivo* during bone mineralization has, however, proved to be a challenging task (7, 9, 11, 14, 20, 22, 23). This is attributed to the very small size of even the mature biomineral particles deposited within a dense organic matrix, their highly substituted structure and poorly crystalline nature, and the difficulty of separating newly formed mineral from the mature crystallites. These difficulties, as well as the transient nature of any precursor phase that might exist, made many of the bulk macroscopic measurements undertaken over the last few decades difficult to interpret unequivocally (10, 12, 13).

Here, we address the issue of the first-formed mineral phase in bone using a biological model system, namely the continuously growing fin bony rays of the Tuebingen long-fin (TL) zebrafish (*Danio rerio*) wild-type line [Zebrafish Information Network (ZFIN) ZFIN ID code ZDB-FISH-990623-2 (Univ of Oregon, Eugene, OR), http://zfin.org/]. The fan-like fin structure is of dermal origin and is supported by acellular skeletal elements called bony rays that form through direct mineralization of type I collagen (24) (Fig. 1*A*). Each ray is composed of two aligned symmetrical elements that are longitudinally segmented (Fig. 1*B*), with the segments held together by massive bundles of collagen fibers forming flexible joints (25).

Fin growth is an active process over the life span of the fish. Longitudinal growth of the fin ray bones occurs by addition of new segments to the distal end of the fin, whereas the proximal segments grow and thicken continuously. The formation of new segments is initiated by the organization of a nonmineralized collagen framework into which the carbonated hydroxyapatite mineral is later deposited (26). Fin growth is governed by two alternating phases: a new bone segment addition phase and a stasis phase. Fin overgrowth in many long-fin strains is achieved by bypassing the stasis phase, such that the fins are, by and large, in a bone growth phase at any given time (27). This offers a unique opportunity for investigating all mineralization stages during normal bone growth within the same animal in a temporally and spatially resolved manner.

Results

Transmission electron microscopy (TEM) examination of the TL fin ray bones using standard thin sections shows that the collagen fibrils are arranged in laterally aligned bundles, and the plate-shaped crystals have their *c*-axes aligned with the fibril axes; they are thus similar to all other bone types up to the level of aligned mineralized collagen fibrils. The nonmineralized matrix is composed of well assembled collagen [supporting information (SI) Fig. S1].

Freshly dissected TL caudal fins observed under a polarized-light microscope in water show an increase in birefringence of the bony rays from the distal end of the fin, where elongation occurs and new bone formation proceeds, toward the proximal end (Fig. 1*A*). An intensity plot of the mineral signal from a microcomputed tomograph generated from x-ray radiographs along the distal part of the fin bony rays shows a linear increase in mineral concentration from the distal end (Fig. 1*C*, gray). The same rays under polarized light do not show a correspondingly linear increase in light intensity with position but, rather, a stepwise increase in the levels of birefringence (Fig. 1*C*, orange). Birefringence could be derived from the collagen fibers and/or

Author contributions: J.M., L.A., and S.W. designed research; J.M. and L.A. performed research; A.S. contributed new reagents/analytic tools; J.M., L.A., and S.W. analyzed data; and J.M., L.A., and S.W. wrote the paper.

The authors declare no conflict of interest.

This article is a PNAS Direct Submission. W.L. is a guest editor invited by the Editorial Board.

‡To whom correspondence should be addressed. E-mail: lia.addadi@weizmann.ac.il.

This article contains supporting information online at www.pnas.org/cgi/content/full/0803354105/DCSupplemental.

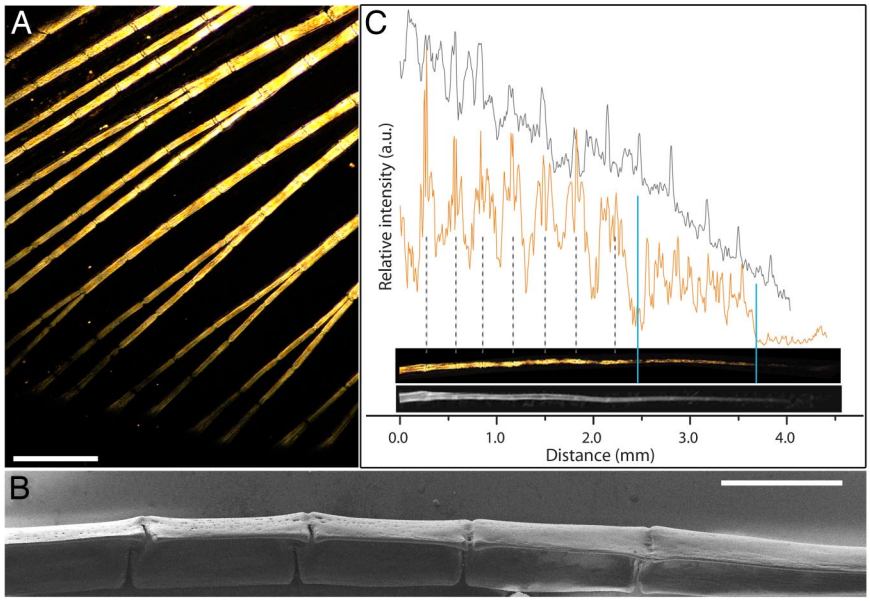

Fig. 1. Polarized-light micrographs, SEM, and micro-CT image of the continuously elongating TL caudal fin. (*A*) Freshly dissected TL caudal fin observed under a polarized-light microscope in water, showing the overall structure of the skeletal elements of the bony rays. An increase in birefringence is observed, starting from the distal end where elongation and new bone formation occur. (Scale bar: 0.5 mm.) (*B*) Scanning electron micrograph of native fin ray segments after the surrounding tissue was removed, dehydrated in an ethanol series, and critical-point dried, showing the half-cylindrical structure of hemisegments that constitute half of the skeletal bony ray. (Scale bar: 200 μm.) (*C*) Intensity plots of birefringence (orange) and mineral density (gray) signals generated from the polarized-light micrograph and micro-CT image, respectively, of a ray shown on the same scale. The dashed lines mark the distinct segments of the ray. Spikes of increased birefringence at the boundaries between segments are due to massive collagen bundles comprising the flexible joints. The blue lines delimit the regions with different signal intensity observed in the birefringence plot.

the crystalline mineral phase and is influenced by the thickness of the specimen. We estimate that, under the conditions used here, the contribution of collagen to the birefringence intensity is minor in view of the fact that the most distal part of the fin, which is composed exclusively of assembled and aligned collagen fibrils, is hardly birefringent (Fig. S1). We regard the lack of correlation between mineral concentration and birefringence observed in the fast forming distal part (see also Fig. S2) as a preliminary indication that a zone of new bone formation exists in which nonbirefringent, and thus noncrystalline, mineral is present.

To investigate this possibility further, we separated the bony rays into distal, middle, and proximal parts representing progressive stages of mineralization. Each part was rapidly frozen in liquid nitrogen and crushed. Observed by high-resolution scanning electron microscopy (SEM), the contours of locally well ordered platy crystallites are barely visible within the organic framework (Fig. 2*A*). Their organization into layers is characteristic of mineralized bone collagen (19, 20). The exposed organic matrix was removed by a brief treatment with sodium hypochlorite, and the mineral was dispersed into small fragments by sonication in ethanol. This enabled high-resolution observation of the mineral particle morphologies by SEM. In the mature proximal segments, mineral particles display the thin platelet-shaped carbonated apatite crystallites characteristic of bone and are clearly arranged in layers (Fig. 2*B*). Very small platelets and spheres are present in the more distal parts of the fin (Fig. 2*C*), and some areas in the most distal segments are composed almost exclusively of spherical particles 10–15 nm in diameter (Fig. 2*D*). At higher resolution, some of the platelet-shaped particles were found to also be composed of small spherical subparticles (Fig. 2*E*). The presence of similar spherical particles, although less abundant, was observed also in particles extracted from fin bones of the more widely used wild-type AB strain of zebrafish (data not shown).

Spherical morphologies are unexpected for crystalline minerals and for crystalline carbonated apatite in particular. They are, however, common in amorphous materials (21). To investigate the nature of these spheres, mineral particles freshly extracted from the distal parts of an elongating caudal fin were deposited on a marked TEM grid. TEM imaging and selected area electron diffraction (SAED) demonstrated that the bone-mineral particles show varying degrees of crystallinity (Fig. 3 *A* and *B*). Some particles (encircled area in Fig. 3*A*) produce diffuse rings in the diffraction pattern, indicating the presence of an amorphous material (Fig. 3*B.a*). Particles composed of aligned elongated plates (area delineated by a rectangle in Fig. 3*A*) produce a poorly crystalline diffraction pattern with the most prevalent diffraction peaks corresponding to the (002) plane of carbonated hydroxyapatite and a broad diffuse ring corresponding to the (112), (211), and (300) reflections (Fig. 3*B.b*). Particles with clear-cut crystalline platelet morphologies (*Inset* in Fig. 3*A*) produce a well defined crystalline diffraction pattern showing the (002) and second-order (004) apatite reflections as well as more defined reflections of the (112), (211), and (300) planes (Fig. 3*B.c*). It is, however, possible that the diffuse diffraction patterns could be derived from nonorganized organic material and not from amorphous mineral. To unequivocally identify the particle composition we thus observed the same particles, uncoated, in the cryo-SEM using a back-scattered electron detector (ESB) (Fig. 3 *C* and *D*). Areas containing mineral particles that produced both amorphous scatter and crystalline diffraction patterns in the TEM showed no distinguishable differences in signal intensities between the crystalline and amorphous particle types when imaged by back-scattered electrons (Fig. 3*D*). This observation demonstrates that the same particles that are amorphous, based on electron diffraction, have a high calcium atomic density of the same order of magnitude as that of the adjacent crystalline mineral particles. They are therefore clearly composed of amorphous mineral. Furthermore, samples kept dry

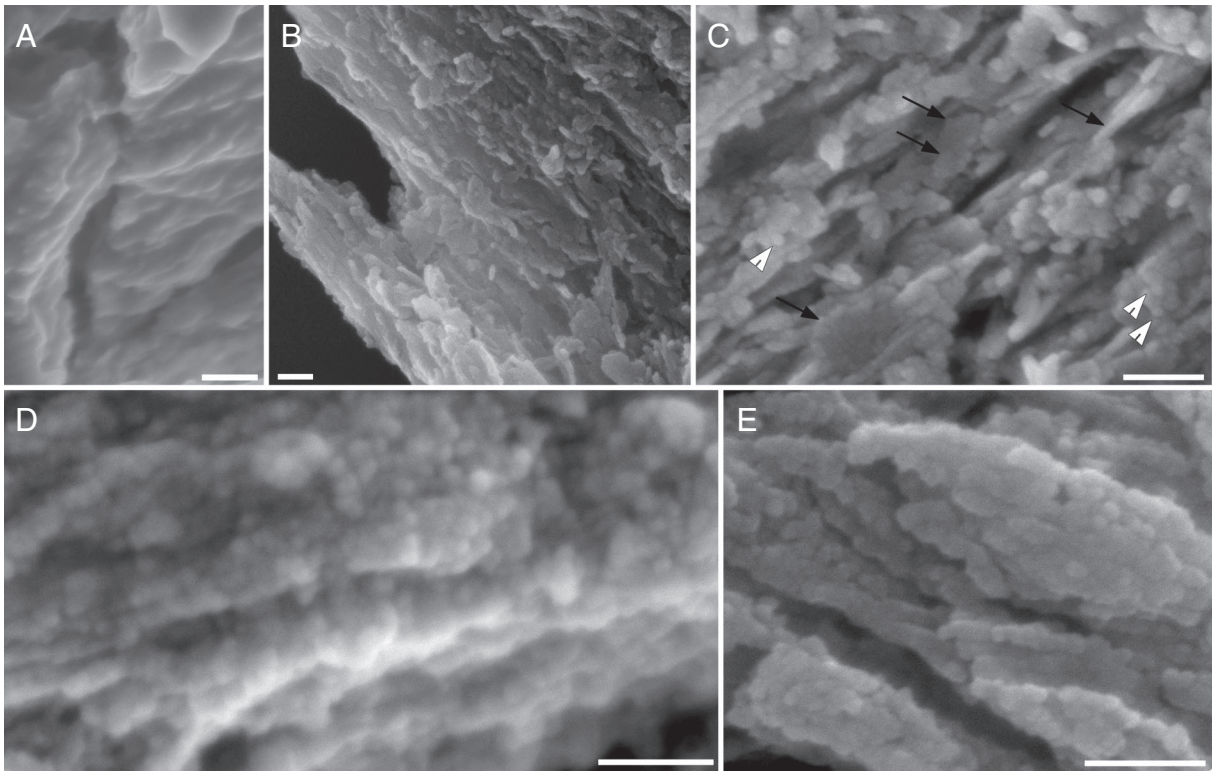

Fig. 2. High-resolution scanning electron micrographs of mineral particle morphologies in different parts along the growing fin bony rays, representing different growth stages. (*A*) Native bony segment showing local layered organization of mineral platelets within the organic matrix. (Scale bar: 200 nm.) (*B*) Proximal, mature bone segment after removal of organic matrix, showing well defined platelet morphology of the carbonated apatite crystallite. (*C*) Coexistent small platelets (black arrows) and spherically shaped mineral particles (white arrowheads) comprise a fragment at a transition zone from mature to growing bone. (*D*) Distal, forming bone segments, almost exclusively composed of dense spherical mineral particles. (*E*) A bone fragment showing that the crystal platelets also appear to be composed of spherical subparticles. (Scale bars in *B–E*: 100 nm.) Samples *B–E* were prepared by washing in acetone, crushing after rapid freezing in liquid nitrogen, removal of organic matrix by immersion in 6% NaOCl, extensive washing, resuspension in ethanol, mounting after evaporation of the ethanol suspension, and coated with 2-nm Cr.

and examined again after incubation at room temperature for a week, showed that some of the particles that originally produced an amorphous diffraction pattern had crystallized, developing detectable (002) diffraction spots (arrowheads in Fig. 3*B.d*).

To measure the atomic composition and stoichiometry of the different types of minerals extracted from the fin bones, the mineral particles were analyzed by using energy-dispersive spectrometry (EDS) in the TEM. This was undertaken to further characterize mineral phases with different degrees of crystallinity, based on their calcium-to-phosphate ratios. The Ca/P ratio was found to span a wide range from 1.1 to 1.8. In addition, the elemental analyses also revealed small amounts of fluoride, magnesium, and other small ions. An average Ca/P ratio of 1.64 ± 0.14 was measured for crystalline mineral particles, whereas an average ratio of 1.34 ± 0.17 was obtained for the amorphous particles. Thus, the bone crystalline mineral phases are similar to stoichiometric crystalline carbonated hydroxyapatite (with a theoretical value of 1.67), and the amorphous phases are similar to synthetic ACP, reported to have ratios of ≈1.35 (21). The wide range of the calcium-to-phosphate ratios measured here correlates well with the different degrees of crystallinities observed in the diffraction patterns (Fig. S3). We estimate that spherical ACP particles in the distal ends of the newly formed bones constitute ≈50% of all of the mineral particles. This is based on counting spherical (amorphous) versus platelet (crystalline) mineral morphologies (22 bone fragments from two caudal fins) in high-resolution SEM images (such as in Fig. 2).

Fourier-transform infrared (FTIR) spectroscopy was used to obtain an independent bulk estimate of the mineral characteristics within the different growth stages along the elongating bony rays. FTIR spectra of mineral extracted from proximal and distal ends of freshly dissected fins are characteristic of carbonated hydroxyapatite (Fig. 4). However, all distal samples have broader phosphate ν_1, ν_3 peaks (at 1,035 cm^{-1}) with more distinct shoulders at ≈1,050 cm^{-1}, 1,150 cm^{-1}, and occasionally at 1,105 cm^{-1}, reminiscent of disordered calcium phosphate and octacalcium phosphate-like phases, as well as a less pronounced peak at 961 cm^{-1} that is characteristic of carbonated hydroxyapatite (22). In addition, a higher carbonate peak (at 872 cm^{-1}) is present in the distal parts. Sample crystallinity was calculated by evaluating the extent of splitting of the phosphate ν_4 absorption peak at 560–600 cm^{-1} (Fig. 4 *Inset*) (7, 8, 28). Calculated splitting factor (SF) values were compared between proximal and distal mineral extracted from the same fin, with proximal mineral always producing higher values of SF (3.11 ± 0.14) than the distal mineral (2.71 ± 0.19) (Fig. 4 *Inset*). This indicates that the bulk young forming bones are composed of mineral particles of low crystallinity, and that mineral crystallinity increases with bone maturation.

Discussion

The zebrafish fin bony rays represent a model system of skeletal bone that has several advantages for studying mineral formation processes. The continuous directional growth in distinct segments provides spatial and temporal resolution of the formation process. Furthermore, bone growth occurs at a lower temperature than in mammals, thus slowing down the transformation kinetics of potential precursor phases into the mature mineral. Based on a combined high-resolution microscopic characterization of particle morphology, diffraction properties, elemental

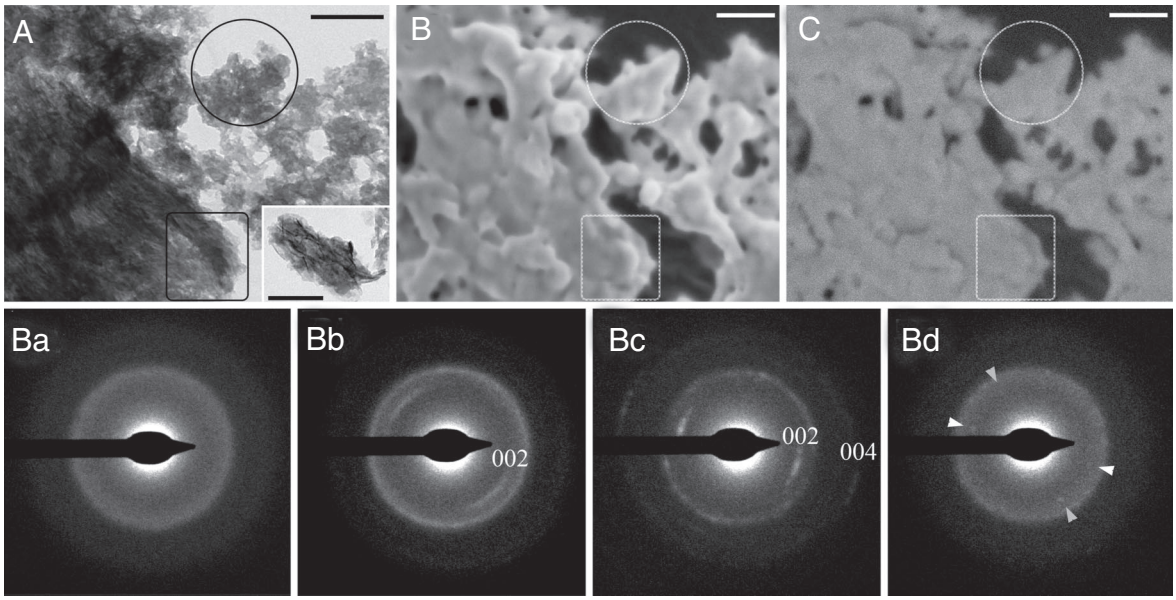

Fig. 3. TEM and SAED correlated with SEM and ESB imaging of mineral freshly extracted from the distal end of the fin. (*A* and *B*) TEM micrograph of mineral particle aggregates and the corresponding SAED patterns: encircled particle produces amorphous scatter of diffuse rings (SAED, *B.a*). Area marked with a rectangle produces poorly crystalline diffraction (SAED, *B.b*), and particle in *Inset* produces a clear crystalline diffraction pattern (SAED, *B.c*), showing well defined reflections of the (002) and second order (004) apatite planes. SAED *B.d* corresponds to the encircled area examined after storage for 1 week at room temperature: As the particles begin to crystallize, diffraction spots with spacing of the (002) plane appear (arrowheads), implying conversion into a crystalline apatite phase. (*C*) High-resolution cryo-SEM micrograph of the same particle, uncoated, taken after examination in the TEM. (*D*) Corresponding ESB image, showing no distinguishable difference between the signal intensity of the amorphous (encircled area) and crystalline (rectangular area) mineral parts. (Scale bars 100 nm.) Samples were prepared by washing in acetone, crushing after rapid freezing in liquid nitrogen, immersion in 6% NaOCl, extensive washing, resuspension in ethanol, sonication, and mounting by evaporating the ethanol suspension on a marked TEM grid.

stoichiometry, and atomic density of minerals freshly extracted from the different fin parts, we were able to demonstrate the presence of an abundant ACP phase in newly formed bones. Our findings indicate that the widely accepted notion that only one mineral phase is present in bone, namely poorly crystalline carbonated hydroxyapatite, is incorrect at least for fin bones. The fact that both amorphous and crystalline minerals are intimately mixed at the nanometer scale as observed in the SEM highlights the difficulties of using bulk measurements, including the FTIR measurements presented here, to monitor transformation processes. Consistent with our observations of a small amount of spherical particles in mature bone of fish fins, Wang *et al.* (29) observed a small proportion of spherical particles in mature baboon bone. Based on ESB images, they concluded that the spherical particles are mineral.

A variety of observations points to the possibility that, over time, the initially deposited ACP transforms into a crystalline mineral phase. As the fin bone matures, the proportion of crystalline mineral increases relative to ACP (Fig. 2). The extracted amorphous particles crystallize with time (Fig. 3). Poorly crystalline mineral particles are observed side by side with amorphous and crystalline particles and are particularly abundant in the transition zone between the forming and the mature parts. This spatial distribution of ACP is consistent with the large-scale changes in birefringence relative to mineral density (Fig. 1*C*) and the changes in the infrared splitting factor, both of which change progressively with position along the ray (Fig. 4).

Fin growth occurs by the *de novo* growth of new mineralized tissue at the distal part of the fin. These new segments thicken during maturation. We suggest that the mineral is first deposited at the growing site in the form of ACP and later transforms into the mature crystalline phase within the collagen fibrils. The transient ACP phase may conceivably be deposited directly inside the gap regions of collagen fibrils, but it may also be delivered as extrafibrillar particles.

In vitro collagen mineralization via a transient ACP precursor phase resulted in the formation of intrafibrillar apatite crystallites reminiscent of natural bone (15). The transient ACP clearly penetrated inside the gap regions of the collagen fibrils, where it crystallized. A different *in vitro* mineralization strategy used double diffusion of ions inside collagen, resulting in slow and controlled formation of oriented OCP crystallites within collagen fibrils (30). These studies are consistent with the possibility that the transient ACP precursor phase may also be deposited directly inside collagen *in vivo*.

Glimcher (1984) (10) noted that even though ACP was certainly not a major stable phase in mature bone, the possibility that it could be a transient precursor phase remained open. Several studies reported the presence of transient precursor calcium phosphate phases involved in the deposition of carbonated hydroxyapatite in different *in vivo* systems. ACP was identified in vesicles associated with cartilage ossification (23), and the presence of an OCP-like precursor phase was detected in mouse calvaria bone mineralization (14). ACP was shown to form as a precursor phase of carbonated hydroxyapatite in chiton teeth (2). We have not found evidence for the presence of any other calcium phosphate phases in the forming fin bone besides ACP and carbonated hydroxyapatite. We note, however, that it is difficult to identify OCP in the presence of carbonated apatite by using the IR spectroscopy and electron diffraction data we have obtained.

Conclusions

Here, we show that a disordered calcium phosphate phase (ACP) is the major mineral phase in the newly formed parts of the fish fin bone. There are several indications that the disordered phase is a precursor of crystalline carbonated hydroxyapatite. This is consistent with other *in vivo* and *in vitro* observations of bone-related mineralization processes as well as diverse observations among invertebrates that amorphous calcium carbonate and

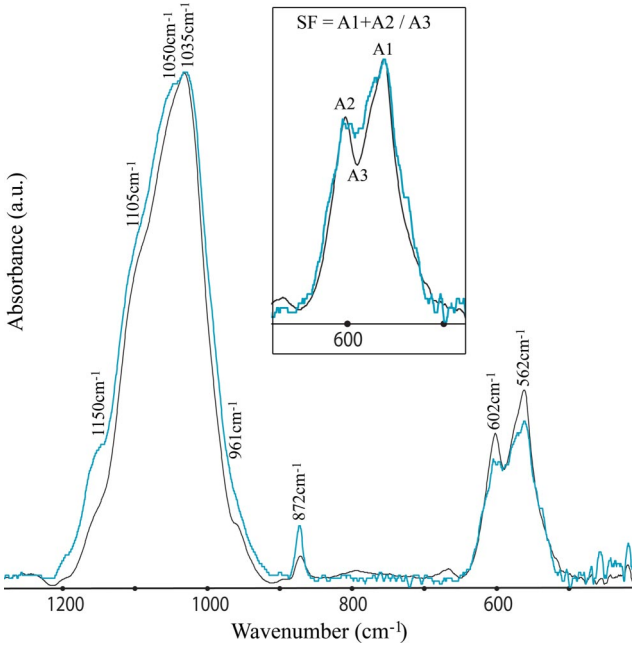

Fig. 4. Representative FTIR spectra of freshly extracted mineral particles from the proximal, mature bone (black) and distal, forming bone (blue) segments of the same fin after removal of the bone organic matrix and sonication into ethanol. The spectra are normalized to the intensity of the phosphate ν_1, ν_3 peak at 1,035 cm^{-1} after baseline correction. (*Inset*) Spectra normalized to the intensity of the 562-cm^{-1} peak. Black: IR spectrum of particles extracted from proximal bone segments; SF = 3.17. Blue: IR spectrum of particles extracted from distal bone segments; SF = 2.58. The difference in SF corresponds to the higher degree of crystallinity of the proximal segments.

amorphous calcium phosphate are precursor phases of the mature crystalline mineral.

Materials and Methods

Mature male zebrafish (*Danio rerio*), ≈1.5 years old, of the Tuebingen long-fin (TL) and AB strains were provided by the courtesy of Gil Levkowitz (Weizmann Institute of Science). The TL strain is a wild-type line homozygous for *leo*^{t1} and *lof*^{dt2}. *leo*^{t1} is a recessive mutation causing spotting in adult fish, also known as *tup*. *lof*^{dt2} is a dominant homozygous viable mutation causing long fins. The AB strain is a widely used wild-type line in which normal, isometric fin growth is maintained [Zebrafish Information Network (ZFIN) ZFIN ID code ZDB-FISH-990623-2 (Univ of Oregon, Eugene, OR), http://zfin.org/]. Freshly dissected caudal fins were used in all experiments.

For observation under a light microscope, whole fins were transferred onto a glass slide, covered with a coverslip, and observed in water by using polarizing-light microscopy (ECLIPSE E600WPOL; Nikon). High-resolution microcomputed tomography images generated from x-ray radiographs were obtained from the same air-dried fresh TL caudal fins (GE Healthcare). Scans were taken at 7-μm isotropic resolution. Maximum-intensity projection images were produced with MicroView software version 5.2.2 (GE Healthcare). Intensity profiles of birefringence from the polarized-light micrographs and mineral signal from the micro-CT radiographs were generated by using ImageJ.

For SEM, bone samples were lightly bleached in 1% sodium hypochlorite for a few seconds to remove nonbone external tissue, washed with Milli-Q water, dehydrated in an ethanol series, (50%, 70%, 96%, and 100%), and then critical-point dried by using a CPD-030 critical-point dryer (Bal-Tec). Some samples were crushed under liquid nitrogen. The dry samples were mounted onto aluminum stubs by using double-sided carbon tape, coated with 2-nm chromium (K757X Chromium Sputterer; Emitech), and visualized in a high-resolution Ultra 55 SEM (Zeiss) using an in-lens secondary electron detector operating at 2 kV.

Mineral Extraction for High-Resolution TEM and SEM and Characterization of Bone Mineral Particles. Freshly dissected caudal fins were extensively washed with acetone to remove fatty tissue components, after which the fins were air dried and further dissected into 3- to 4-mm proximal, middle, and distal regions, each corresponding to 10–15 rays' long parts. Each of the different fin parts was processed separately by freezing with liquid nitrogen and crushing in an agate mortar. Sodium hypochlorite solution (6%) was added for 5 minutes at room temperature while manually stirring the suspension. The suspension was then transferred into Eppendorf tubes and centrifuged at 14,000 rpm for 2 min (Eppendorf 5417C microcentrifuge) to remove the supernatant. The pellet was washed three times with Milli-Q water saturated with calcium and phosphate and twice with 100% ethanol. The pellet was resuspended in ethanol and sonicated (Ultrasonicprocessor W-380; Heat Systems Ultrasonics) with three 10- to 30-sec. pulses of high intensity. For both SEM and TEM, the mineral suspension was deposited on a marked TEM grid by evaporating a drop of the ethanol suspension. The extraction procedure was completed within 30 min per sample. The procedure was tested on synthetically precipitated ACP; a highly metastable mineral phase, and found to not alter the mineral phase, as determined by IR spectroscopy and high-resolution SEM.

TEM Imaging, Electron Diffraction, and Elemental Analysis. Samples were observed within a few hours after mineral extraction by using an FEI (Philips) T120-Technai TEM operating at 120 kV. The electron diffraction patterns of the particles were recorded by using a selected-area aperture allowing observation of a circular area of 200-nm diameter. Caution was taken regarding the size and thickness of the examined aggregates, because these parameters may influence the quality of the diffraction patterns. The grid was then stored at room temperature, observed in the SEM, and observed again after 1 week in the TEM.

EDS of equivalent samples was performed by using a Philips CM120 Super Twin TEM (120 kV, tungsten/LaB6). Calcium-to-phosphate ratios were calculated as the ratio between the atomic percentages of the two elements. The electron diffraction patterns of the particles were also recorded. Forty mineral aggregates from five different preparations were analyzed for correlations of the electron diffraction patterns and calcium-to-phosphate ratios.

Cryo-SEM and ESB Imaging. The marked TEM grid on which freshly extracted mineral particles were deposited and previously observed in the TEM was transferred to an Ultra 55 SEM (Zeiss). The same mineral particles previously analyzed by electron diffraction were identified and observed uncoated at a temperature of −120°C by using an in-lens secondary electron detector and a back-scattered electron in-lens detector, operating at 1 kV and an ESB grid voltage operating at 300 V. Stronger signals in the back-scattered images are obtained from the higher-atomic-mass elements, i.e., calcium atoms within the mineral phase, providing information regarding the atomic density relative to the organic and crystalline material within the sample examined. The back-scattered electrons signal was first adjusted with reference to the carbon-coated membrane previously deposited on the grid support, because no clear tissue organic residues were detected. Keeping the imaging conditions constant, the previously examined mineral aggregates were imaged. These observations were made on six large mineral aggregates each containing a number (2–4) of areas with mineral particles with different crystallinities, including amorphous particles. Equivalent samples of mineral extracts from different positions along the bony rays were also observed after coating with 2-nm chromium in a K757X Chromium Sputterer (Emitech) and visualized in a high-resolution Ultra 55 SEM (Zeiss) by using an in-lens secondary electron detector operating at 2 kV.

IR Spectroscopy and Calculation of the Phosphate ν_4 SF. Freshly extracted mineral suspensions (prepared as described above) were transferred to an agate mortar where the ethanol was removed by exposure to a heat lamp for ≈30 seconds. The residual material was lightly crushed, and a 7-mm KBr pellet was prepared. The spectra were recorded by using a Nicolet 380 FTIR spectrometer at 1-cm^{-1} resolution averaging over 32 scans. Background KBr was measured in advance and then used for base-line correction for the sample spectra. The sample spectra were often noisy because of the very small sample size. Thus, all sample spectra were smoothed to the same extent (10 cm^{-1}). The spectra were then normalized to the intensity of the 562-cm^{-1} peak, and the SF of the phosphate ν_4 antisymmetric bending frequency at 560–600 cm^{-1} was calculated as the sum of the ≈562-cm^{-1} and ≈600-cm^{-1} peak heights divided by the height of the minimum between this doublet following Weiner and Bar-Yosef (28). Calculated SF values were compared between proximal and distal mineral extracted from the same fin. Five such sets were measured.

ACKNOWLEDGMENTS. We thank Dr. Gil Levkowitz for providing the animals. The electron microscopy studies were conducted at the Irving and Cherna Moskowitz Center for Nano and Bio-Nano Imaging, Weizmann Institute of Science. L.A. is the incumbent of the Dorothy and Patrick Gorman Professorial Chair of Biological Ultrastructure, and S.W. is the incumbent of the Dr. Trude Burchardt Professorial Chair of Structural Biology. J.M. was supported by fellowships from the Israel Ministry of Science and Education and the Israeli Council for Higher Education. This work was supported by a grant from the Minerva Foundation.

1. Towe KM, Lowenstam HA (1967) Ultrastructure and development of iron mineralization in the radular teeth of *Cryptochiton stelleri* (Mollusca). *J Ultrastructure Res* 17:1–13.
2. Lowenstam HA, Weiner S (1985) Transformation of amorphous calcium phosphate to crystalline dahillite in the radular teeth of chitons. *Science* 227:51–53.
3. Beniash E, Aizenberg J, Addadi L, Weiner S (1997) Amorphous calcium carbonate transforms into calcite during sea-urchin larval spicule growth. *Proc R Soc London Ser B* 64:461–465.
4. Hasse B, *et al.* (2000) Calcium carbonate modifications in the mineralized shell of the freshwater snail *Biomphalaria glabrata. Chem Eur J* 6:3679–3685.
5. Weiss IM, Tuross N, Addadi L, Weiner S (2002) Mollusk larval shell formation: amorphous calcium carbonate is a precursor for aragonite. *J Exp Zool* 293:478–491.
6. Politi Y, *et al.* (2004) Sea urchin spine calcite forms via a transient amorphous calcium carbonate phase. *Science* 306:1161–1164.
7. Termine JD, Posner AS (1966) Infrared analysis of rat bone: Age dependency of amorphous and crystalline mineral fractions. *Science* 153:1523–1525.
8. Termine JD, Posner AS (1966) Infra-red determination of the percentage of crystallinity in apatitic calcium phosphates. *Nature* 211:268–270.
9. Brown WE, Chow LC (1976) Chemical properties of bone mineral. *Annu Rev Mat Sci* 6:213–236.
10. Glimcher MJ (1984) Recent studies of the mineral phase in bone and its possible linkage to the organic matrix by protein-bound phosphate bonds. *Philos Trans R Soc London Ser B* 304:479–508.
11. Bonucci E (1992) in *Calcification of Biological Systems*, ed Bonucci E (CRC, Boca Raton, FL), p 19.
12. Weiner S (2006) Transient precursor strategy in mineral formation of bone. *Bone* 39:431–433.
13. Grynpas MD, Omelon S (2007) Transient precursor strategy or very small biological apatite crystals? *Bone* 41:162–164.
14. Crane NJ, *et al.* (2006) Raman spectroscopic evidence for octacalcium phosphate and other transient mineral species deposited during intramembranous mineralization. *Bone* 39:434–442.
15. Olszta MJ, *et al.* (2007) Bone structure and formation: A new perspective. *Mat Sci Eng R* 58:77–116.
16. De Jong WF (1926) The mineral substance in bone (translated from French). *Rec Trav Chim Pays-Bas* 45:445–448.
17. Weiner S, Price P (1986) Disaggregation of bone into crystals. *Calcif Tissue Int* 39:365–375.
18. Fitton Jackson S (1956) The fine structure of developing bone in the embryonic fowl. *Proc R Soc London Ser B* 146:270–280.
19. Traub W, Arad T, Weiner S (1989) Three dimensional ordered distribution of crystals in turkey tendon collagen fibers. *Proc Natl Acad Sci USA* 86:9822–9826.
20. Landis WJ, *et al.* (1996) Structural relations between collagen and mineral in bone as determined by high voltage electron microscopic tomography. *Microsc Res Tech* 33:192–202.
21. Christoffersen J, Christoffersen MR, Kibalczyc W, Andersen FA (1989) A contribution to the understanding of the formation of calcium phosphates. *J Cryst Growth* 94:767–777.
22. Sauer GR, Wuthier RE (1988) Fourier-transform infrared characterization of mineral phases formed during induction of mineralization by collagenase-released matrix vesicles *in vitro. J Biol Chem* 263:13718–13724.
23. Wu LN, *et al.* (1997) Physicochemical characterization of the nucleational core of matrix vesicles. *J Biol Chem* 272:4404–4411.
24. Bird NC, Mabee PM (2003) Developmental morphology of the axial skeleton of the zebrafish, *Danio rerio* (Ostariophysi: Cyprinidae). *Dev Dyn* 228:337–357.
25. Montes GS, *et al.* (1982) Fine structure and histochemistry of the tail fin ray in teleosts. *Histochemistry* 75:363–376.
26. Landis WJ, Geraudie J (1990) Organization and development of the mineral phase during early ontogenesis of the bony fin rays of the trout *Oncorhynchus mykiss. Anat Rec* 228:383–391.
27. Goldsmith MI, Fisher S, Waterman R, Johnson SL (2003) Saltatory control of isometric growth in the zebrafish caudal fin is disrupted in *long fin* and *rapunzel* mutants. *Dev Biol* 259:303–317.
28. Weiner S, Bar-Yosef O (1990) States of preservation of bones from prehistoric sites in the Near East: A survey. *J Archaeol Sci* 17:187–196.
29. Wang L, *et al.* (2006) Nanosized particles in bone and dissolution insensitivity of bone mineral. *Biointerphases* 1:106–111.
30. Iijima M, Iijima K, Moriwaki Y, Kuboki Y (1994) Oriented growth of octacalcium phosphate crystals on type-I collagen fibrils under physiological conditions. *J Cryst Growth* 140:91–99.